# Pose Estimation with Lidar Odometry and Cellular Pseudoranges

Joe Khalife[1], Sonya Ragothaman[1], and Zaher M. Kassas[2]

*Abstract*— A pose estimation framework by fusing light de-tection and ranging (lidar) odometry measurements and cellular pseudoranges using an extended Kalman filter is proposed. Iterative closest point (ICP) is used to solve for the relative pose between lidar scans. A maximum likelihood estimator is developed for lidar scan registration. The proposed framework works with few ICP iterations; hence, can be used for real-time applications. The framework is tested experimentally, and it is demonstrated that the two-dimensional position root mean square error obtained with ICP only can be reduced by 93.58% by fusing lidar odometry and cellular pseudoranges.

## I. INTRODUCTION

Light detection and ranging (lidar) sensors can be used for mapping [1]–[3] or for odometry measurements by solving for the relative pose between consecutive scans [4]–[6]. The vehicle's trajectory can be reconstructed by combining these odometry measurements. This approach suffers from two main challenges: (1) the pose estimation error will drift over time, rendering the estimate unreliable and (2) the reconstructed trajectory will be in a local frame that is not necessarily aligned with the global frame. The first challenge is inherent to all dead-reckoning (DR) systems. For lidar sensors, this drift can be reduced by pre-processing the scans and smoothing the estimate over the trajectory [7], [8]. This however increases the computational burden and does not allow for real-time implementations. One way to correct for this drift is to use GPS measurements which provide a pose estimate with respect to a global frame [9]. However, GPS signals may become unreliable in environments such as indoor or deep urban environments, where GPS coverage is sparse. In contrast, signals of opportunity (SOPs), such as cellular, digital television, and AM/FM radio, have a high received power in urban environments compared to GPS signals. Research in exploitation of such signals for navigation has revealed their potential as an alternative or complement to GPS [10]–[13]. In [14], cellular signals were used to aid an inertial navigation system (INS) in the absence of GPS and establish bounds on the estimation error.

One challenge for using cellular signals for navigation is the unavailability of published receiver architectures that are capable of extracting navigation observables from these signals. Recently, software-defined radio (SDR) architectures were proposed for extracting pseudorange measurements from CDMA [12] and LTE [13] signals. In cellular net-works, base stations, referred to as base transceiver stations

(BTSs) in CDMA systems and eNodeBs in LTE systems, are assigned a unique ID which can be decoded by the receiver [12], [13]. Subsequently, the receiver can lookup the coordinates of the BTS or eNodeB from which it is drawing pseudorange measurements, either from a local or cloud-hosted database, and solve for its position in the global frame. These coordinates could be obtained in various ways, including surveying, satellite imagery, or radio mapping [15], [16]. While the position of the BTSs or eNodeBs are fixed and could be stored in a database and made available to the navigating receiver, the BTSs or eNodeBs clock error states (bias and drift) are dynamic and stochastic; therefore, they must be continuously estimated.

This paper considers the following problem. A moving vehicle equipped with a two-axis lidar sensor and a cellular SOP receiver (CDMA and LTE) is estimating its pose in an outdoor environment. The objective is two-fold. First, the fusion of lidar odometry and cellular pseudoranges is investigated and the resulting pose estimation performance is assessed. Second, the performance gain over using lidar odometry only is studied. The vehicle is equipped with an integrated GPS-inertial navigation system (GPS-INS) to produce ground truth results. Lidar odometry is obtained by registering consecutive three–dimensional (3–D) laser scans using an iterative closest point (ICP) approach [17]. Although ICP has a closed form solution for the relative pose, it does not employ an optimal estimator nor returns an estimate of the estimation error covariance [18], which is important when fusing the lidar odometry measurements with cellular SOPs.

This paper makes two contributions. First, a framework for fusing lidar odometry measurements and cellular pseu-doranges using an extended Kalman filter (EKF) is proposed. Second, a maximum likelihood 3–D laser scan registration method is proposed, which also estimates the covariance of the relative pose estimation error. This will be useful when propagating the covariance of the absolute pose estimation error in the EKF. Experimental results show that the proposed framework reduces the 2–D position root mean square error (RMSE) of the ICP only method by 93.58%.

The remainder of the paper is organized as follows. Sec-tion II gives an overview of the framework and provides all the model descriptions. Section III discusses lidar odometry and a maximum likelihood approach for point registration. Section IV presents the EKF model for fusing lidar odometry and cellular pseudoranges. Section V provides experimental results that show a vehicle estimating its pose using real lidar measurements and real cellular signals. Section VI gives concluding remarks.

[1] Graduate student, Department of Electrical & Computer Engineer-ing, University of California, Riverside, USA, jkhal001@ucr.edu, srago001@ucr.edu.
[2] Assistant professor, Department of Electrical & Computer Engineering, University of California, Riverside, USA, zkassas@ieee.org.

## II. FRAMEWORK OVERVIEW AND MODEL DESCRIPTION

This section gives an overview of the framework and presents the dynamics model of the vehicle-mounted receiver and cellular SOP as well as the measurement model of the lidar and the cellular pseudoranges.

### A. Framework Overview

The paper considers the following problem. A moving vehicle equipped with a (1) lidar sensor and (2) cellular receiver is present in a cellular SOP environment with known transmitter locations. The vehicle is estimating its own pose and the clock biases and clock drifts of the receiver and cellular SOPs' clock error states. The lidar sensor is used for odometry measurements and the cellular receiver is producing cellular pseudorange measurements. The odometry and pseudorange measurements are fused in an EKF. An ICP algorithm is employed to find the relative pose of the vehicle between consecutive lidar scans. This relative pose is used as an odometry measurement to propagate the global pose of the vehicle. The cellular receiver is producing pseudorange measurements to $N_s$ ambient cellular SOPs with known transmitter locations. These pseudoranges are used to update the pose estimate. The pose estimation framework is illustrated in Fig. 1.
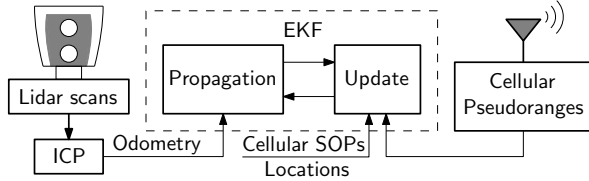


Fig. 1. Framework for pose estimation with lidar odometry and cellular pseudoranges.

### B. SOP Dynamics Model

The cellular SOPs emanate from spatially-stationary terrestrial BTSs or eNodeBs, and their states will consist of their known 3-D positions and unknown clock error states, namely the clock bias and clock drift. Hence, the state of the $n$-th SOP is given by $\boldsymbol{x}_{s_n} = \left[ \boldsymbol{r}_{s_n}^\mathsf{T}, \boldsymbol{x}_{\mathrm{clk},s_n}^\mathsf{T} \right]^\mathsf{T}$, where $\boldsymbol{r}_{s_n} = [x_{s_n}, y_{s_n}, z_{s_n}]^\mathsf{T}$ is the 3-D position vector of the $n$-th BTS or eNodeB and $\boldsymbol{x}_{\mathrm{clk},s_n} \triangleq \left[ c\delta t_{s_n}, c\dot{\delta} t_{s_n} \right]^\mathsf{T}$ is the clock error state of the $n$-th cellular SOP where $\delta t_{s_n}$ and $\dot{\delta} t_{s_n}$ are the clock bias and clock drift, respectively, and $c$ is the speed-of-light. The $n$-th cellular SOP's dynamics can be described by the discrete-time (DT) state space model

$$\boldsymbol{x}_{s_n}(k+1) = \mathbf{F}_s \, \boldsymbol{x}_{s_n}(k) + \boldsymbol{w}_{s_n}(k), \quad n = 1, \ldots, N_s,$$

where $\mathbf{F}_s = \mathrm{diag}\left[ \mathbf{I}_{2\times 2}, \mathbf{F}_{\mathrm{clk}} \right]$, $\boldsymbol{w}_{s_n}$ is a DT zero-mean white noise sequence with covariance $\mathbf{Q}_{s_n} = \mathrm{diag}\left[ \mathbf{0}_{2\times 2}, \mathbf{Q}_{\mathrm{clk},s_n} \right]$,

$$\mathbf{F}_{\mathrm{clk}} = \begin{bmatrix} 1 & T \\ 0 & 1 \end{bmatrix}, \quad \mathbf{Q}_{\mathrm{clk},s_n} = c^2 \begin{bmatrix} S_{\delta t_{s_n}} T + S_{\dot{\delta} t_{s_n}} \frac{T^3}{3} & S_{\dot{\delta} t_{s_n}} \frac{T^2}{2} \\ S_{\dot{\delta} t_{s_n}} \frac{T^2}{2} & S_{\dot{\delta} t_{s_n}} T \end{bmatrix},$$

where $T$ is the sampling time and $S_{\delta t_{s_n}}$ and $S_{\dot{\delta} t_{s_n}}$ are the power spectra of the process noise of the clock bias and clock drift, respectively. These spectra can be related to the power-law coefficients $\{h_\alpha\}_{\alpha=-2}^2$, which have been shown through laboratory experiments to be adequate to characterize the power spectral density of the fractional frequency deviation $y(t)$ of an oscillator from nominal frequency, which takes the form $S_y(f) = \sum_{\alpha=-2}^2 h_\alpha f^\alpha$ [19]. It is common to approximate the clock error dynamics by considering only the frequency random walk coefficient $h_{-2}$ and the white frequency coefficient $h_0$, which lead to $S_{\delta t_{s_n}} \approx \frac{h_{0,s_n}}{2}$ and $S_{\dot{\delta} t_{s_n}} \approx 2\pi^2 h_{-2,s_n}$.

### C. Vehicle-Mounted Receiver Dynamics Model

The state of the vehicle-mounted navigating receiver is given by $\boldsymbol{x}_r \triangleq \left[ \boldsymbol{x}_B^\mathsf{T}, \boldsymbol{x}_{\mathrm{clk},r}^\mathsf{T} \right]^\mathsf{T}$, where $\boldsymbol{x}_B$ is the vehicle's pose and $\boldsymbol{x}_{\mathrm{clk},r} \triangleq \left[ c\delta t_r, c\dot{\delta} t_r \right]^\mathsf{T}$ is the receiver's clock error state. The vehicle's pose is given by

$$\boldsymbol{x}_B \triangleq \left[ {}_B^G \boldsymbol{q}^\mathsf{T}, \boldsymbol{r}_r^\mathsf{T} \right]^\mathsf{T},$$

where ${}_B^G \boldsymbol{q}$ is the 4-D unit quaternion vector in vector-scalar form that represents the orientation of the vehicle's body $B$ in a global frame $G$ (e.g., the Earth-centered Earth-fixed (ECEF) coordinate frame) and $\boldsymbol{r}_r = [x_r, y_r, z_r]^\mathsf{T}$ is the 3-D position of the vehicle in the global frame. The orientation of the vehicle will evolve in DT according to the kinematic model given by

$$ {}_{B_{k+1}}^G \boldsymbol{q} = {}_{B_k}^G \boldsymbol{q} \otimes {}_{B_{k+1}}^{B_k} \boldsymbol{q}, \tag{1}$$

where ${}_{B_k}^G \boldsymbol{q}$ represents the orientation of the vehicle body frame in the global frame at time $k$, ${}_{B_{k+1}}^{B_k} \boldsymbol{q}$ represents the relative rotation of the vehicle body frame from time-step $k$ to $k+1$, and $\otimes$ is the quaternion multiplication operator. The vehicle's position evolves according to the kinematic model given by

$$\boldsymbol{r}_r(k+1) = \boldsymbol{r}_r(k) + \mathbf{R}\left[ {}_{B_k}^G \boldsymbol{q} \right] {}^{B_k}\boldsymbol{r}_{B_{k+1}}, \tag{2}$$

where $\mathbf{R}[\boldsymbol{q}]$ is the 3-D rotation matrix constructed from the 4-D quaternion vector $\boldsymbol{q}$ and ${}^{B_k}\boldsymbol{r}_{B_{k+1}}$ is the position of the vehicle at time $k+1$ expressed in the vehicle body frame at time $k$, i.e., ${}^{B_k}\boldsymbol{r}_{B_{k+1}}$ represents the vehicle's translation between time steps $k$ and $k+1$. The receiver's clock state evolves according to the same DT model as the cellular SOP's clock state, except that $h_{0,s_n}$ and $h_{-2,s_n}$ are now replaced with $h_{0,r}$ and $h_{-2,r}$, respectively.

### D. Clock State Difference Dynamics

Although the SOP locations are assumed to be known, their clock states are unknown, dynamic, and stochastic; hence, they must be estimated continuously. A pseudorange can be parameterized by the difference between the receiver's and the SOP's clock biases [20]. Therefore, one only needs to estimate the difference in clock biases and clock drifts $\boldsymbol{\Delta x}_{\mathrm{clk}_n}$, specifically

$$\boldsymbol{\Delta x}_{\mathrm{clk}_n} \triangleq \boldsymbol{x}_{\mathrm{clk},r} - \boldsymbol{x}_{\mathrm{clk},s_n} = \left[ c\Delta\delta t_n, c\Delta\dot{\delta} t_n \right]^\mathsf{T},$$

where $\Delta\delta t_n \triangleq \delta t_r - \delta t_{s_n}$ and $\Delta\dot{\delta} t_n \triangleq \dot{\delta} t_r - \dot{\delta} t_{s_n}$. The set of clock state differences $\Delta\boldsymbol{x}_{\text{clk}} \triangleq \left[\Delta\boldsymbol{x}_{\text{clk}_1}^{\mathsf{T}}, \ldots, \Delta\boldsymbol{x}_{\text{clk}_{N_s}}^{\mathsf{T}}\right]^{\mathsf{T}}$ can be expressed as

$$\Delta\boldsymbol{x}_{\text{clk}} = \mathbf{T}\boldsymbol{x}_{\text{clk}},$$

$$\boldsymbol{x}_{\text{clk}} \triangleq \begin{bmatrix} \boldsymbol{x}_{\text{clk},r} \\ \boldsymbol{x}_{\text{clk},s_1} \\ \vdots \\ \boldsymbol{x}_{\text{clk},s_{N_s}} \end{bmatrix}, \quad \mathbf{T} \triangleq \begin{bmatrix} \mathbf{I} & -\mathbf{I} & \mathbf{0} & \ldots & \mathbf{0} \\ \mathbf{I} & \mathbf{0} & -\mathbf{I} & \ldots & \mathbf{0} \\ \vdots & \vdots & \vdots & \ddots & \vdots \\ \mathbf{I} & \mathbf{0} & \mathbf{0} & \ldots & -\mathbf{I} \end{bmatrix},$$

where $\mathbf{I}$ is the $2 \times 2$ identity matrix. Subsequently, the dynamics of $\Delta\boldsymbol{x}_{\text{clk}}$ in DT is given by

$$\Delta\boldsymbol{x}_{\text{clk}}(k+1) = \boldsymbol{\Phi}_{\text{clk}}\Delta\boldsymbol{x}_{\text{clk}}(k) + \boldsymbol{w}_{\text{clk}}(k), \quad (3)$$

where $\boldsymbol{\Phi}_{\text{clk}} \triangleq \text{diag}\left[\mathbf{F}_{\text{clk}}, \ldots, \mathbf{F}_{\text{clk}}\right]$ and $\boldsymbol{w}_{\text{clk}}$ is a zero-mean DT random vector with covariance $\mathbf{Q}_{\text{clk}} = \mathbf{T}\,\mathbf{Q}_{\text{clk},r,s}\mathbf{T}^{\mathsf{T}}$, where $\mathbf{Q}_{\text{clk},r,s} \triangleq \text{diag}\left[\mathbf{Q}_{\text{clk},r}, \mathbf{Q}_{\text{clk},s_1}, \ldots, \mathbf{Q}_{\text{clk},s_{N_s}}\right]$.

### E. Lidar Measurement Model

Each lidar scan consists of relative position measurements to $L$ points in the environment. The relative position measurement to the $i$-th point can be expressed as

$$\boldsymbol{z}_{l_i}(k) = {}^{B_k}\boldsymbol{r}_{l_i} + \boldsymbol{v}_{l_i}(k), \quad (4)$$

where ${}^{B_k}\boldsymbol{r}_{l_i}$ is the 3-D position of the $i$-th point expressed in the vehicle body frame at time step $k$ and $\boldsymbol{v}_{l_i}$ is the measurement noise, which is modeled as a zero-mean Gaussian random vector with $\mathbb{E}\left[\boldsymbol{v}_{l_i}(k)\,\boldsymbol{v}_{l_i}^{\mathsf{T}}(k')\right] = \mathbf{C}_{l_i}\,\delta_{kk'}$, where $\delta_{kk'}$ is the Kronecker delta function.

### F. Cellular Pseudorange Measurement Model

The cellular pseudorange measurement made by the receiver on the $n$-th SOP BTS or eNodeB, after discretization and mild approximations discussed in [20], is given by

$$z_{s_n}(k) = \left\| \boldsymbol{r}_r(k) - \boldsymbol{r}_{s_n}(k) \right\|_2 + c\Delta\delta t_n(k) + v_{s_n}, \quad (5)$$

where $v_{s_n}$ is the measurement noise, which is modeled as a DT zero-mean white Gaussian sequence with variance $\sigma_{s_n}^2$.

## III. Lidar Odometry

This section describes the steps for producing odometry data, namely the relative pose of the vehicle between lidar scans.

### A. ICP Algorithm

The ICP algorithm and its variants involve two main steps at their core: (1) finding the point correspondence and (2) registering the corresponding points [17]. ICP algorithms are iterative, i.e., given an initial relative pose guess, steps (1) and (2) are repeated until convergence. In this paper, a simple approach is employed for step (1), which is the mutual consistency check: given two sets of scans $\mathcal{P}^k$ and $\mathcal{P}^{k+1}$, and two points $\boldsymbol{p}_i^k \in \mathcal{P}^k$ and $\boldsymbol{p}_{i'}^{k+1} \in \mathcal{P}^{k+1}$, then $\boldsymbol{p}_i^k$ and $\boldsymbol{p}_{i'}^{k+1}$ are corresponding points if

$$\underset{\boldsymbol{p}_j^k \in \mathcal{P}^k}{\arg\min}\left\| \boldsymbol{p}_{i'}^{k+1} - \boldsymbol{p}_j^k \right\|_2 = \boldsymbol{p}_i^k \text{ and } \underset{\boldsymbol{p}_j^{k+1} \in \mathcal{P}^{k+1}}{\arg\min}\left\| \boldsymbol{p}_i^k - \boldsymbol{p}_j^{k+1} \right\|_2 = \boldsymbol{p}_{i'}^{k+1}.$$

There exists several methods to perform step (2) [4], [6]. In this paper, a maximum likelihood approach for registering the points is developed.

### B. Point Registration Using Maximum Likelihood Estimation

The parameters to be estimated are $\boldsymbol{x}_l \triangleq \left[{}^{B_k}_{B_{k+1}}\boldsymbol{q}^{\mathsf{T}}, {}^{B_k}\boldsymbol{r}_{B_{k+1}}^{\mathsf{T}}\right]^{\mathsf{T}}$. After determining the point correspondence, the following relation holds

$$ {}^{B_k}\boldsymbol{r}_{l_i} = {}^{B_k}\boldsymbol{r}_{B_{k+1}} + \mathbf{R}_k {}^{B_{k+1}}\boldsymbol{r}_{l_i}, \quad (6)$$

where $\mathbf{R}_k \triangleq \mathbf{R}\left[{}^{B_k}_{B_{k+1}}\boldsymbol{q}\right]$. Consequently, the relative position measurement to the $i$-th feature can aslo be expressed as

$$\boldsymbol{z}_{l_i}(k) = {}^{B_k}\boldsymbol{r}_{B_{k+1}} + \mathbf{R}_k\,\boldsymbol{z}_{l_i}(k+1) + \boldsymbol{v}_{l_i}(k) - \mathbf{R}_k\,\boldsymbol{v}_{l_i}(k+1).$$

Given the estimate $\hat{\boldsymbol{x}}_l \triangleq \left[{}^{B_k}_{B_{k+1}}\hat{\boldsymbol{q}}^{\mathsf{T}}, {}^{B_k}\hat{\boldsymbol{r}}_{B_{k+1}}^{\mathsf{T}}\right]^{\mathsf{T}}$, the measurement estimate can be expressed as

$$\hat{\boldsymbol{z}}_{l_i}(k) = {}^{B_k}\hat{\boldsymbol{r}}_{B_{k+1}} + \hat{\mathbf{R}}_k\,\boldsymbol{z}_{l_i}(k+1),$$

where $\hat{\mathbf{R}}_k \triangleq \mathbf{R}\left[{}^{B_k}_{B_{k+1}}\hat{\boldsymbol{q}}\right]$. The residual $\boldsymbol{\nu}_{l_i}(k) \triangleq \boldsymbol{z}_{l_i}(k) - \hat{\boldsymbol{z}}_{l_i}(k)$ is therefore given by

$$\boldsymbol{\nu}_{l_i}(k) = {}^{B_k}\tilde{\boldsymbol{r}}_{B_{k+1}} + \tilde{\mathbf{R}}_k\,\boldsymbol{z}_{l_i}(k+1) + \boldsymbol{n}_i(k),$$

where ${}^{B_k}\tilde{\boldsymbol{r}}_{B_{k+1}} \triangleq {}^{B_k}\boldsymbol{r}_{B_{k+1}} - {}^{B_k}\hat{\boldsymbol{r}}_{B_{k+1}}$, $\tilde{\mathbf{R}}_k \triangleq \mathbf{R}_k - \hat{\mathbf{R}}_k$, and $\boldsymbol{n}_i \triangleq \boldsymbol{v}_{l_i}(k) - \mathbf{R}_k\,\boldsymbol{v}_{l_i}(k+1)$ is a DT zero-mean Gaussian random vector with covariance approximated by $\mathbf{C}_{n_i}(k) = \mathbf{C}_{l_i} + \hat{\mathbf{R}}_k\mathbf{C}_{l_i}\hat{\mathbf{R}}_k^{\mathsf{T}}$. Using the small angle approximation, the rotation matrix $\mathbf{R}_k$ can be approximated with

$$\mathbf{R}_k \approx \left(\mathbf{I} + \lfloor\tilde{\boldsymbol{\theta}}_l\times\rfloor\right)\hat{\mathbf{R}}_k, \quad (7)$$

where $\tilde{\boldsymbol{\theta}}_l$ is the 3-axis error vector and $\lfloor\boldsymbol{v}\times\rfloor$ is the skew-symmetric matrix formed by vector $\boldsymbol{v} \in \mathbb{R}^3$. Hence, the residual can be expressed as

$$\begin{aligned} \boldsymbol{\nu}_{l_i}(k) &\approx {}^{B_k}\tilde{\boldsymbol{r}}_{B_{k+1}} + \lfloor\tilde{\boldsymbol{\theta}}_l\times\rfloor\hat{\mathbf{R}}_k\,\boldsymbol{z}_{l_i}(k+1) + \boldsymbol{n}_i(k) \\ &= {}^{B_k}\tilde{\boldsymbol{r}}_{B_{k+1}} - \lfloor\hat{\mathbf{R}}_k\,\boldsymbol{z}_{l_i}(k+1)\times\rfloor\tilde{\boldsymbol{\theta}}_l + \boldsymbol{n}_i(k) \\ &= \mathbf{H}_{l_i}\,\tilde{\boldsymbol{x}}_l + \boldsymbol{n}_i(k), \end{aligned}$$

$$\mathbf{H}_{l_i} \triangleq \begin{bmatrix} -\lfloor\hat{\mathbf{R}}_k\,\boldsymbol{z}_{l_i}(k+1)\times\rfloor & \mathbf{I} \end{bmatrix}, \quad \tilde{\boldsymbol{x}}_l \triangleq \begin{bmatrix} \tilde{\boldsymbol{\theta}}_l \\ {}^{B_k}\tilde{\boldsymbol{r}}_{B_{k+1}} \end{bmatrix}.$$

Since the lidar measurement noise is Gaussian and independent, then maximizing the likelihood function will be equivalent to

$$\underset{\tilde{\boldsymbol{x}}_l}{\text{minimize}} \sum_{i=1}^{N_p} \boldsymbol{\nu}_{l_i}^{\mathsf{T}}(k)\,\mathbf{C}_{n_i}^{-1}(k)\boldsymbol{\nu}_{l_i}(k),$$

where $N_p$ is the total number of corresponding points. This minimization step is performed iteratively (Gauss-Newton method) until the estimates converge, and the estimates are updated after each iteration according to

$$\begin{aligned} {}^{B_k}\hat{\boldsymbol{r}}_{B_{k+1}}^{(t+1)} &= {}^{B_k}\hat{\boldsymbol{r}}_{B_{k+1}}^{(t)} + {}^{B_k}\tilde{\boldsymbol{r}}_{B_{k+1}}^{(t)}, \\ {}^{B_k}_{B_{k+1}}\hat{\boldsymbol{q}}^{(t+1)} &= {}^{B_k}_{B_{k+1}}\tilde{\boldsymbol{q}}^{(t)} \otimes {}^{B_k}_{B_{k+1}}\hat{\boldsymbol{q}}^{(t)}, \end{aligned}$$

where $_{B_{k+1}}^{B_k}\tilde{q}^{(t)} \triangleq \left[\frac{1}{2}\left(\tilde{\theta}_l^{(t)}\right)^\mathsf{T}, \sqrt{1-\frac{1}{4}\left(\tilde{\theta}_l^{(t)}\right)^\mathsf{T}\tilde{\theta}_l^{(t)}}\right]^\mathsf{T}$, and

$\tilde{\theta}_l^{(t)}$ and $_{B_{k+1}}^{B_k}\tilde{r}_{B_{k+1}}^{(t)}$ are the corrections computed at iteration $t$ according to

$$\begin{bmatrix} \tilde{\theta}_l^{(t)} \\ _{B_{k+1}}^{B_k}\tilde{r}_{B_{k+1}}^{(t)} \end{bmatrix} = \mathbf{Q}_l^{(t)}\left[\sum_{i=1}^{N_p}\left(\mathbf{H}_{l_i}^{(t)}\right)^\mathsf{T}\left(\mathbf{C}_{n_i}^{(t)}(k)\right)^{-1}\nu_{l_i}(k)\right],$$

where $\mathbf{Q}_l^{(t)} = \left[\sum_{i=1}^{N_p}\left(\mathbf{H}_{l_i}^{(t)}\right)^\mathsf{T}\left(\mathbf{C}_{n_i}^{(t)}(k)\right)^{-1}\mathbf{H}_{l_i}^{(t)}\right]^{-1}$ and $\mathbf{H}_{l_i}^{(t)} = \left[-\lfloor\mathbf{R}\left[_{B_{k+1}}^{B_k}\hat{q}^{(t)}\right]z_{l_i}(k+1)\times\rfloor \quad \mathbf{I}\right]$. After convergence, an estimate $\hat{x}_l = \left[_{B_{k+1}}^{B_k}\hat{q}^\mathsf{T}, ^{B_k}\hat{r}_{B_{k+1}}^\mathsf{T}\right]^\mathsf{T}$ is obtained. The resulting estimation error $\tilde{x}_l = \left[\tilde{\theta}_l^\mathsf{T}, ^{B_k}\tilde{r}_{B_{k+1}}^\mathsf{T}\right]^\mathsf{T}$ is zero-mean and has a covariance $\mathbf{Q}_l$.

## IV. EKF MODEL

In this section, the EKF framework that fuses lidar odometry and cellular pseudoranges is developed.

### A. State Vector and EKF Error State Model

The state vector $x$ comprises the vehicle's pose and the differences of clock error states, i.e., $x \triangleq \left[x_B^\mathsf{T}, \Delta x_{\mathrm{clk}}^\mathsf{T}\right]^\mathsf{T}$. The EKF produces an estimate $\hat{x}(k|k) \triangleq \mathbb{E}\left[x(k)\middle|\{z_s(j)\}_{j=1}^k\right]$ of $x(k)$, and an associated estimation error covariance $\mathbf{P}(k|k) \triangleq \mathbb{E}\left[\tilde{x}(k|k)\,\tilde{x}^\mathsf{T}(k|k)\right]$ where $z_s \triangleq \left[z_{s_1}, \ldots, z_{s_{N_s}}\right]^\mathsf{T}$. The error state $\tilde{x}$ is defined as

$$\tilde{x} = \left[\tilde{x}_B^\mathsf{T}, \tilde{\Delta}x_{\mathrm{clk}}^\mathsf{T}\right]^\mathsf{T},$$

where $\tilde{x}_B = \left[\tilde{\theta}^\mathsf{T}, \tilde{r}_r^\mathsf{T}\right]^\mathsf{T}$. The position and clock errors are defined as the standard additive error, i.e., $\tilde{r}_r \triangleq r_r - \hat{r}_r$ and $\tilde{\Delta}x_{\mathrm{clk}} \triangleq \Delta x_{\mathrm{clk}} - \hat{\Delta}x_{\mathrm{clk}}$. The orientation error is related through the quaternion product

$$_B^G q = \delta q \otimes {_B^G}\hat{q}, \tag{8}$$

where the error quaternion $\delta q$ is the small deviation of the estimate $_B^G\hat{q}$ from the true orientation $_B^G q$ and is given by $\delta q = \left[\frac{1}{2}\tilde{\theta}^\mathsf{T}, \sqrt{1-\frac{1}{4}\tilde{\theta}^\mathsf{T}\tilde{\theta}}\right]^\mathsf{T}$. Similarly to (7), this error can be used to approximate the true orientation with

$$\mathbf{R}\left[_B^G q\right] \approx \left(\mathbf{I} + \lfloor\tilde{\theta}\times\rfloor\right)\mathbf{R}\left[_B^G\hat{q}\right].$$

### B. State Estimate and Covariance Propagation

The propagation of the state estimate follows directly from (1), (2), and (3), i.e.,

$$_{B_{k+1|k}}^G\hat{q} = {_{B_{k|k}}^G}\hat{q} \otimes {_{B_{k+1}}^{B_k}}\hat{q}, \tag{9}$$

$$\hat{r}_r(k+1|k) = \hat{r}_r(k|k) + \mathbf{R}\left[_{B_{k|k}}^G\hat{q}\right]^{B_k}\hat{r}_{B_{k+1}}, \tag{10}$$

$$\hat{\Delta}x_{\mathrm{clk}}(k+1|k) = \mathbf{\Phi}_{\mathrm{clk}}\hat{\Delta}x_{\mathrm{clk}}(k|k), \tag{11}$$

where $_{B_{k+1}}^{B_k}\hat{q}$ and $^{B_k}\hat{r}_{B_{k+1}}$ are obtained from the ICP algorithm discussed in Section III. By linearizing equations (9)–(11) around the state estimate, it can be shown that the error state dynamics can be approximated with

$$\tilde{x}_B(k+1|k) \approx \mathbf{\Phi}_B\tilde{x}_B(k|k) + \mathbf{G}_l\tilde{x}_l(k), \tag{12}$$

$$\mathbf{\Phi}_B \triangleq \begin{bmatrix} \mathbf{I} & \mathbf{0} \\ -\lfloor\hat{\mathbf{R}}_{B_k}{^{B_k}}\hat{r}_{B_{k+1}}\times\rfloor & \mathbf{I} \end{bmatrix}, \quad \mathbf{G}_l \triangleq \begin{bmatrix} \hat{\mathbf{R}}_{B_k} & \mathbf{0} \\ \mathbf{0} & \hat{\mathbf{R}}_{B_k} \end{bmatrix},$$

where $\hat{\mathbf{R}}_{B_k} = \mathbf{R}\left[_{B_{k|k}}^G\hat{q}\right]$. The overall estimation error covariance is propagated according to

$$\mathbf{P}_{k+1|k} = \mathbf{\Phi}\mathbf{P}_{k|k}\mathbf{\Phi}^\mathsf{T} + \mathbf{G}\mathbf{Q}\mathbf{G}^\mathsf{T},$$

$$\mathbf{\Phi} = \begin{bmatrix} \mathbf{\Phi}_B & \mathbf{0} \\ \mathbf{0} & \mathbf{\Phi}_{\mathrm{clk}} \end{bmatrix}, \quad \mathbf{G} = \begin{bmatrix} \mathbf{G}_l & \mathbf{0} \\ \mathbf{0} & \mathbf{I} \end{bmatrix}, \quad \mathbf{Q} = \begin{bmatrix} \mathbf{Q}_l & \mathbf{0} \\ \mathbf{0} & \mathbf{Q}_{\mathrm{clk}} \end{bmatrix}.$$

### C. State and Covariance Update

The measurement prediction is given by

$$\hat{z}_{s_n}(k+1|k) = \|\hat{r}_r(k+1|k) - r_{s_n}\|_2 + c\hat{\Delta}\delta t_n(k+1|k).$$

Therefore, the innovation vector is calculated according to

$$\nu_s(k+1|k) = z_s(k+1) - \hat{z}_s(k+1|k),$$

where $\hat{z}_s(k+1|k) \triangleq \left[\hat{z}_{s_1}(k+1|k), \ldots, \hat{z}_{s_{N_s}}(k+1|k)\right]^\mathsf{T}$. The Kalman gain $\mathbf{K}$ is computed according to

$$\mathbf{K} = \mathbf{P}_{k+1|k}\mathbf{H}_s^\mathsf{T}\mathbf{S}^{-1},$$

where $\mathbf{S} = \mathbf{H}_s\mathbf{P}_{k+1|k}\mathbf{H}_s^\mathsf{T} + \mathbf{\Sigma}_s$ is the innovation covariance and $\mathbf{\Sigma}_s = \mathrm{diag}\left[\sigma_{s_1}^2, \ldots, \sigma_{s_{N_s}}^2\right]$ is the measurement noise covariance. The measurement Jacobian $\mathbf{H}_s$ is taken with respect to the error state and is given by

$$\mathbf{H}_s \triangleq [\mathbf{H}_{\mathrm{qp}} \quad \mathbf{H}_{\mathrm{clk}}], \quad \mathbf{H}_{\mathrm{qp}} \triangleq \left[h_{\mathrm{qp}_1} \quad \ldots \quad h_{\mathrm{qp}_{N_s}}\right]^\mathsf{T},$$

$$\mathbf{H}_{\mathrm{clk}} \triangleq \mathrm{diag}\left[h_{\mathrm{clk}}^\mathsf{T}, \ldots, h_{\mathrm{clk}}^\mathsf{T}\right], \quad h_{\mathrm{qp}_n} \triangleq \left[0_{1\times 3} \quad 1_{s_n}^\mathsf{T}\right]^\mathsf{T},$$

$$1_{s_n} \triangleq \left[\frac{(\hat{r}_r(k+1|k) - r_{s_n})}{\|\hat{r}_r(k+1|k) - r_{s_n}\|_2}\right], \quad h_{\mathrm{clk}} \triangleq \begin{bmatrix}1 & 0\end{bmatrix}^\mathsf{T}.$$

The position and clock states are updated by adding the corresponding correction terms obtained by multiplying the innovation vector by the Kalman gain. The orientation state is updated similarly to (8), where the left quaternion vector is obtained from the correction terms corresponding to the orientation state.

## V. EXPERIMENTAL RESULTS

In this section, experimental results showing a car navigating with lidar odometry and cellular pseudoranges are presented.

### A. Experimental Setup

A car was equipped with a Velodyne HDL-64E lidar sensor. The lidar has a 360-degree field of view in the azimuth and a vertical field of view of +2 degrees to -8.33 degrees, and was set to rotate at 15 Hz. Each laser scan returns 88,889 points in 3–D space. In order to achieve real-time, each third scan is processed and only 0.5% of the total points in each scan are used. Moreover, since large planar areas degrade the ICP solution, the points that are too close

to the ground (within 50 cm) were discarded. The ground plane, which is assumed to remain constant in the lidar frame, was calculated prior to the experiment. An average of 380 points per scan remain after the selection. An example of this point selection scheme is shown in Fig. 2.
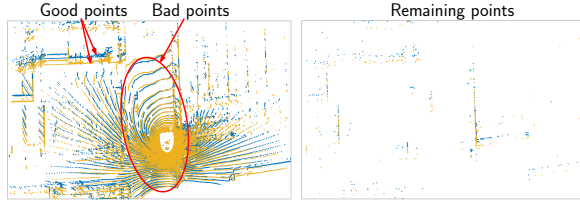


Fig. 2. Example of the point selection scheme from lidar scans.

The car was also equipped with two cellular antennas to acquire and track signals from nearby: (a) cellular CDMA BTSs and (b) LTE eNodeBs. The CDMA and LTE antennas used for the experiment were consumer-grade 800/1900 MHz cellular antennas. The signals were simultaneously down-mixed and synchronously sampled via National Instruments's (NI) dual-channel universal software radio peripheral (USRP) RIO, driven by a GPS-disciplined oscillator (GSPDO). The receivers were tuned to the cellular carrier frequency 882.75 MHz for CDMA, which is a channel allocated for U.S. cellular provider Verizon Wireless, and 1955 MHz for LTE, which is a channel allocated for U.S. cellular provider AT&T. Samples of the received signals were stored for off-line post-processing. The SDRs developed in [12] and [13] were used to produce cellular pseudoranges. Over the course of the experiment, the vehicle-mounted receiver was listening to the same 3 cellular SOPs: 2 CDMA BTSs and 1 LTE eNodeB with known positions. Fig. 3 shows the experimental hardware setup, the environment layout, and the true trajectory traversed by the car.
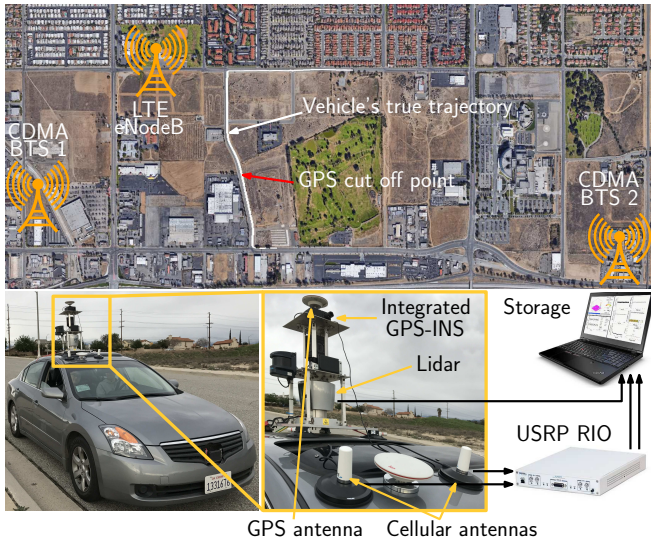


Fig. 3. A car was equipped with a lidar sensor, an integrated GPS-INS, cellular antennas and a USRP. The car traversed a suburban area collecting GPS, lidar, and inertial measurement unit (IMU) measurements and cellular SOP signals from two CDMA BTSs and one LTE eNodeB.

The true trajectory of the car was obtained from an independent on-board integrated GPS–INS. The car traversed a total trajectory of 1.454 Km. To simulate a GPS cut off, the navigation solution obtained from the integrated GPS–INS was used for the first 454 m only, and for the remaining 1 Km of the total trajectory, it was assumed that the car had access only to lidar data and pseudorange measurements to three cellular SOPs. While GPS signals were not used in the EKF for estimating the pose of the car, they were still used by the on-board integrated GPS–INS to get the ground truth. The state of the vehicle right before GPS was cut off was used to initialize the EKF.

*B. Results*

Fig. 4 shows pose estimation results using ICP only and using ICP and three cellular SOPs. The number of iterations in the Gauss-Newton solver was set to 5, which is the number of iterations usually required by the algorithm to converge, and the maximum number of iterations in the ICP algorithm was set to 40. The ICP program ran at half the real-time speed. The RMSE using ICP only was found to be 150.20 m for the 3–D position, whereas the RMSE using ICP and 3 cellular SOPs was 29.63 m. The RMSE of the 2–D position ($x\,y$ RMSE) was 149.72 m for ICP only and 9.61 m for ICP and 3 cellular SOPs. The small vertical positioning error resulting from using ICP only is justified by the small variation in the vertical direction of the car's trajectory. In contrast, when using ICP and cellular SOPs, the vertical error becomes significant, which is due to the poor vertical dilution of precision inherent to terrestrial SOPs (there is minimal diversity in the BTSs' and eNodeB's vertical positions). However, using cellular SOPs reduced the 2–D RMSE to less than 6.7% of the 2–D RMSE obtained using ICP only. The 2–D solution is more precise in this case since the horizontal dilution of precision is very good (there is a significant diversity in the BTSs' and eNodeB's 2–D positions). Subsequently, a 2–D position was obtained using ICP and three cellular SOPs. In this case, the height of the car was assumed to be known and constant. The 2–D RMSE using ICP only was calculated to be 151.18 m, whereas the 2–D RMSE using ICP and 3 cellular SOPs was 8.21 m.
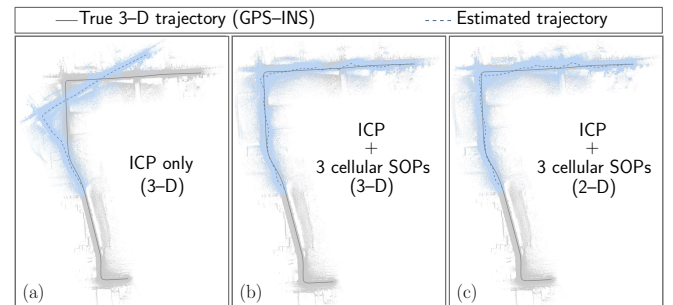


Fig. 4. Experimental results showing the true vehicle 3–D trajectory and the estimated vehicle trajectory: (a) 3–D solution using ICP only, (b) 3–D solution using ICP and three cellular SOPs, and (c) 2–D solution using ICP and three cellular SOPs.

Next, the proposed framework was tested in 2–D space only by varying the maximum number of iterations in the ICP algorithm. Fig. 5 shows the 2–D solutions, and the RMSE

values are summarized in Table I. It can be seen from Fig. 5 and Table I that while the quality of the ICP only solution varies dramatically with the maximum number of iterations, it does not change much when three cellular SOPs are used. Moreover, the program ran in real-time for a maximum of 10 iterations or less.
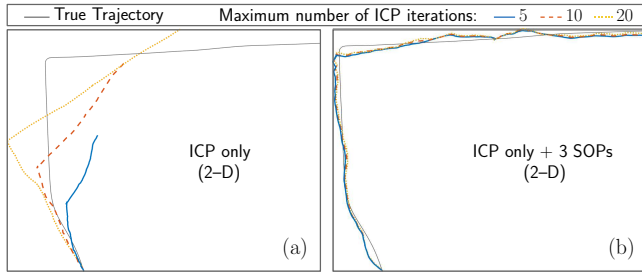


Fig. 5. Experimental results showing (a) the 2–D solution using ICP only and (b) the 2–D solution using ICP and three cellular SOPs for 5, 10, and 20 maximum ICP iterations.

TABLE I

SUMMARY OF EXPERIMENTAL RESULTS

| Max. number of ICP iterations | 2–D RMSE (m) | |
| | ICP only | ICP + 3 cellular SOPs |
| --- | --- | --- |
| 5 | 287.94 | 10.22 |
| 10 | 218.05 | 9.07 |
| 20 | 171.6 | 8.50 |
| 40 | 151.18 | 8.21 |

## VI. CONCLUSION

A framework for pose estimation that fuses lidar odometry and cellular pseudoranges was proposed. The framework consists of an EKF that uses lidar odometry to propagate the pose of the vehicle and uses cellular pseudoranges to update the estimates in order to: (1) eliminate the drift arising from integrating noisy odometry measurements and (2) provide an absolute pose estimate in a global frame. An ICP algorithm is employed to extract odometry measurements from lidar scans. A simple mutual consistency check is used to establish point correspondence. Subsequently, a maximum likelihood approach for registering lidar scans is developed. This method also allows the estimation of the covariance of the odometry data estimation error, which is important for propagating the pose estimation error covariance in the EKF. Moreover, experimental results demonstrating the proposed framework are presented. Over a 1 Km trajectory, the 2–D RMSE of the ICP only solution was 151.18 m, whereas the 2–D RMSE of ICP and 3 cellular pseudoranges was 8.21 m. Experimental results show that reducing the maximum number of ICP iterations does not have a considerable effect on the ICP and cellular solution, whereas this degrades the ICP only solution dramatically.

## ACKNOWLEDGMENT

## REFERENCES

[1] S. Rodriguez, V. Fremont, P. Bonnifait, and V. Cherfaoui, "An embedded multi-modal system for object localization and tracking," in *Proceedings of IEEE Intelligent Vehicles Symposium*, June 2010, pp. 211–216.

[2] G. Trehard, E. Pollard, B. Bradai, and F. Nashashibi, "On line mapping and global positioning for autonomous driving in urban environment based on evidential slam," in *Proceedings of IEEE Intelligent Vehicles Symposium*, June 2015, pp. 814–819.

[3] T. Gee, J. James, W. V. D. Mark, P. Delmas, and G. Gimel'farb, "Lidar guided stereo simultaneous localization and mapping (SLAM) for UAV outdoor 3-D scene reconstruction," in *International Conference on Image and Vision Computing*, November 2016, pp. 1–6.

[4] W. Choi, Y. Kim, S. Oh, and J. Lee, "Fast iterative closest point framework for 3D LIDAR data in intelligent vehicle," in *Proceedings of IEEE Intelligent Vehicles Symposium*, June 2012, pp. 1029–1034.

[5] J. Zhang and S. Singh, "Visual-lidar odometry and mapping: low-drift, robust, and fast," in *Proceedings of IEEE International Conference on Robotics and Automation*, May 2015, pp. 2174–2181.

[6] J. Rohde, B. Volz, H. Mielenz, and J. Zollner, "Precise vehicle localization in dense urban environments," in *Proceedings of IEEE International Conference on Intelligent Transportation Systems*, November 2016, pp. 853–858.

[7] G. Grisetti, S. Grzonka, C. Stachniss, P. Pfaff, and W. Burgard, "Efficient estimation of accurate maximum likelihood maps in 3D," in *IEEE/RSJ International Conference on Intelligent Robots and Systems*, November 2007, pp. 3472–3478.

[8] A. Nuchter, J. Elseberg, P. Schneider, and D. Paulus, "Linearization of rotations for globally consistent n-scan matching," in *Proceedings of IEEE International Conference on Robotics and Automation*, May 2010, pp. 7888–7894.

[9] A. Soloviev, "Tight coupling of GPS, laser scanner, and inertial measurements for navigation in urban environments," in *Proceedings of IEEE/ION Position, Location and Navigation Symposium*, May 2008, pp. 145–152.

[10] C. Yang, T. Nguyen, and E. Blasch, "Mobile positioning via fusion of mixed signals of opportunity," *IEEE Aerospace and Electronic Systems Magazine*, vol. 29, no. 4, pp. 34–46, April 2014.

[11] J. Morales, J. Khalife, and Z. Kassas, "GNSS vertical dilution of precision reduction using terrestrial signals of opportunity," in *Proceedings of ION International Technical Meeting Conference*, January 2016, pp. 664–669.

[12] J. Khalife, K. Shamaei, and Z. Kassas, "A software-defined receiver architecture for cellular CDMA-based navigation," in *Proceedings of IEEE/ION Position, Location, and Navigation Symposium*, April 2016, pp. 816–826.

[13] K. Shamaei, J. Khalife, and Z. Kassas, "Performance characterization of positioning in LTE systems," in *Proceedings of ION GNSS Conference*, September 2016, pp. 2262–2270.

[14] J. Morales, P. Roysdon, and Z. Kassas, "Signals of opportunity aided inertial navigation," in *Proceedings of ION GNSS Conference*, September 2016, pp. 1492–1501.

[15] Z. Kassas, V. Ghadiok, and T. Humphreys, "Adaptive estimation of signals of opportunity," in *Proceedings of ION GNSS Conference*, September 2014, pp. 1679–1689.

[16] J. Morales and Z. Kassas, "Optimal receiver placement for collaborative mapping of signals of opportunity," in *Proceedings of ION GNSS Conference*, September 2015, pp. 2362–2368.

[17] P. Besl and N. Mckay, "A method for registration of 3-D shapes," *IEEE Transactions on Pattern Analysis and Machine Intelligence*, vol. 14, no. 2, pp. 239–256, February 1992.

[18] J. Williams and M. Bennamoun, "A multiple view 3D registration algorithm with statistical error modeling," *IEICE Transactions on Information and Systems*, vol. 83, no. 8, pp. 1662–1670, August 2000.

[19] A. Thompson, J. Moran, and G. Swenson, *Interferometry and Synthesis in Radio Astronomy*, 2nd ed. John Wiley & Sons, 2001.

[20] Z. Kassas and T. Humphreys, "Observability analysis of collaborative opportunistic navigation with pseudorange measurements," *IEEE Transactions on Intelligent Transportation Systems*, vol. 15, no. 1, pp. 260–273, February 2014.